Wear 426–427 (2019) 1466–1473

Contents lists available at ScienceDirect

Wear

journal homepage: www.elsevier.com/locate/wear

Sliding wear of a self-mated thermally sprayed chromium oxide coating in a simulated PWR water environment

V.L. Ratia[a], D. Zhang[a], J.L. Daure[a], P.H. Shipway[a,*], D.G. McCartney[a], D.A. Stewart[b]

[a] Faculty of Engineering, University of Nottingham, University Park, Nottingham, UK
[b] Rolls-Royce plc, Raynesway, Derby, UK

ARTICLE INFO

Keywords:
Ceramic
Tribocorrosion
Nuclear
Surface engineering
Chromia
Cr_2O_3

ABSTRACT

Bearing surfaces in the primary circuit of pressurised water reactors (PWR) are prone to damage due to aggressive chemical and tribological conditions under which they operate, and a wide range of materials have been examined in this regard. One of the most promising candidates is chromium oxide in the form of a thermally spayed coating, and in this work, the behaviour of a commercially available Cr_2O_3 coating in self-mated sliding was considered. Tests consisted of a number of start-stop cycles of sliding between a crowned pin and a rotating disc in a water environment in an autoclave in an attempt to simulate the most aggressive phase of bearing run-up and run-down. Wear and damage mechanisms were examined at temperatures from ambient up to 250 °C (a representative PWR environment). Samples were characterised before and after wear testing using mass measurements, profilometry, X-ray diffraction, scanning and transmission electron microscopy (SEM and TEM) and X-ray photoelectron spectroscopy (XPS).

Across the temperature range, wear was mild, with no evidence of coating delamination. A five-fold increase in wear was observed between 80 °C and 250 °C (with wear depths of generally less than 8 μm being observed on the disc samples even at the higher temperature), despite there being only very small changes in hardness of the coating over the same temperature range. Debris was observed on the wear tracks following testing, with the evidence together suggesting that this debris was a very fine-grained mixture of Cr_2O_3 and amorphous γ-CrOOH, a corrosion product of Cr_2O_3.

1. Introduction

Components such as valves and bearings operating in the primary circuit of pressurised water reactors (PWRs) are required to exhibit both wear and corrosion resistance. Whilst ceramics are not generally considered as structural components, surface engineering with ceramic materials can potentially provide desirable performance due to their high hardness, wear resistance, chemical stability and oxidation-resistance at high temperatures [1–6]. However, whilst many ceramic materials are not chemically stable in the PWR operating environment (including alumina), chromium oxide (Cr_2O_3) is considered to be stable and is thus considered a candidate material for surface engineering of structural components for use in such environments.

Plasma spraying of ceramics is widely used in industry to provide mechanical, thermal and corrosion protection to components in a broad range of applications, including aerospace and automotive applications and alongside aluminium oxide, chromium oxide is one of the most commonly employed ceramic materials for wear resistant thermally sprayed coatings [2,6]. Chromium oxide (Cr_2O_3, eskolaite) coatings have been shown to exhibit excellent wear and friction characteristics, ease of lubrication, high melting temperature (around 2435 °C), resistance to galvanic and high temperature corrosion and are commonly used in the automotive industry on piston rings and cylinder liners [1,4,6–8]. The friction and wear characteristics of plasma sprayed Cr_2O_3 coatings are significantly affected by the porosity of the coating, the presence of microcracks and the adhesion of the coating to the substrate [1,8]. Previous studies have investigated the wear characteristics of plasma sprayed Cr_2O_3 in unlubricated and lubricated sliding conditions, at room temperature and up to 800 °C [6,8,9]. These studies have described the presence of smooth tribofilms on the worn surfaces, formed by plastic deformation of compacted debris. These films are reported to comprise of CrO_2 and CrO_3 and are said to significantly affect the friction and wear characteristics of the coating [5,6,8–10]. It is reported that, at room temperature, CrO_3 dominates whereas at the higher temperature of 450 °C, CrO_2 is observed. These films are reported to decrease the friction coefficient of the coating

* Corresponding author.
E-mail address: philip.shipway@nottingham.ac.uk (P.H. Shipway).

https://doi.org/10.1016/j.wear.2018.12.058
Received 30 August 2018; Received in revised form 13 December 2018; Accepted 20 December 2018

during sliding; however, the films are observed to be thicker at room temperature than at the higher temperature [8–10].

Chromium oxide is generally observed to be chemically stable, and thus it is seen as a strong candidate as a wear resistant material in PWR conditions (water temperatures of up to around 300 °C). However, it is not inert under these conditions; chromium containing alloys are known to form passivating films of Cr_2O_3 and CrOOH (both chromium (III) compounds) in high temperature water, but as the pH and temperature increase, the tendency for soluble Cr(VI) species to form instead is increased, resulting in the loss of any passivation [11]. In exposure of pure chromium in high temperature water, the formation of the amorphous chromium (III) compound, γ-CrOOH has been observed at temperatures as low as 250 °C [12]. Furthermore, it has been shown that this amorphous form is the stable form of CrOOH in water at temperatures up to 300 °C, with the crystalline forms being stable at higher temperatures [13]. As well as being formed on metal surfaces exposed to high temperature solutions, CrOOH has also been observed on the surface of a Cr_2O_3 powder bed following exposure in high temperature phosphate and hydroxide solutions in an autoclave at temperatures up to 288 °C [14].

Whilst the wear behaviour and hydrothermal corrosion behaviour of chromium oxide are well documented, it is also well understood that in situations where there is both corrosion and wear, the two material removal processes do not act independently of each other. As such, as candidate enhanced materials are sought for bearing surfaces to operate in PWR primary loops, the tribocorrosion behaviour of commercially available thermally sprayed Cr_2O_3 coating will be examined in sliding in simulated PWR water as a function of temperature.

2. Experimental procedures

2.1. Preparation of coated test specimens

The wear testing was conducted in a pin-on-disc configuration, with both the pins and discs being manufactured from 316 stainless steel. The discs were 30 mm in diameter and 10 mm in thickness, and pins had a diameter of 10 mm and height of 13 mm. For both the pin and disc specimens, one of the plane surfaces was coated with chromium oxide by thermal spraying by a commercial supplier (Praxair Surface Technologies) to a target thickness of ~ 250 μm. Following coating, the coated disc surfaces were ground to a surface finish (Ra) of approximately 0.4 μm, with this resulting in a final coating thickness of ~ 150 μm. The grinding of the coated surface of the pin was used to both deliver the required surface finish and to develop the geometrical form of a spherical cap with a radius of 50 mm; the thickness of the coating on the axis of the pin (i.e. at the centre of the cap) was ~ 200 μm, with this reducing with distance from the axis resulting in a small rim around the edge of the spherical cap where the coating had been entirely removed.

Coated low-carbon steel coupons were used for determining porosity, adhesion C633 tests and microhardness measurements, and some of the characterisation.

2.2. Autoclave wear testing

Wear testing was conducted in an autoclave pin-on-disc wear tester (previously described in [15]) which allows testing to be conducted at elevated temperatures in an aqueous environment. In the test setup, shown in Fig. 1, the disc is mounted in a rotating sample holder, and the spherical cap end of the pin is loaded against the rotating disc via a 4 kgf stainless steel dead load contained within the autoclave itself. Buoyancy effects on the dead loading result in small changes in contact load with temperature as a result of changes in the densities of both the water and the steel; the contact force varies between ~ 35 N and 37 N across the temperature range. The rotation of the disc is driven through a magnetic coupling with an external drive. The offset of the axis of loading and the axis of rotation is 10 mm, resulting in a wear track diameter of 20 mm and a sliding speed of 0.21 m s^{-1} at the maximum rotational speed of 200 r.p.m.

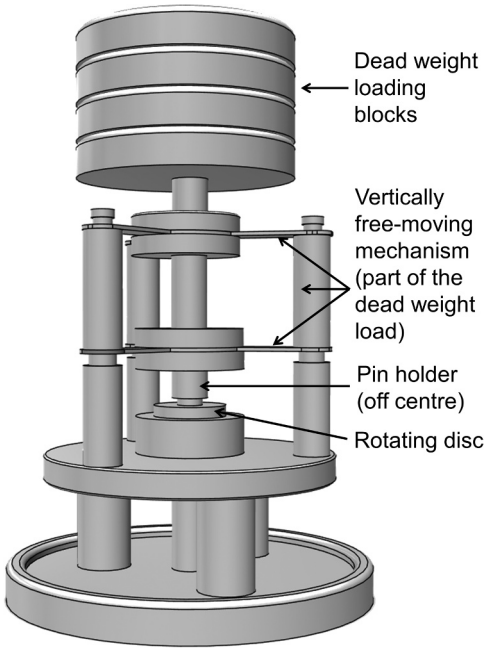

Fig. 1. Schematic diagram of the pin-on-disc apparatus which is enclosed in an autoclave for wear testing [15].

The wear test system is immersed in deoxygenated deionised water with an addition of 8.5 mg of LiOH per litre resulting in initial pH of approximately 10.5 at room temperature. Just before the test, the water is deoxygenated by purging of oxygen-free nitrogen gas into the water for 15 min. As a result, the oxygen content of the water is reduced to less than 1.5 ppm. A range of water temperatures (measured via a thermowell inside the autoclave) were employed as follows: room temperature (~ 20 °C), 80 °C, and 250 °C. The pressure in the system was built up autogenously (i.e. no external pressurisation was employed).

The parameters of the wear test are presented in Table 1. In an attempt to simulate the conditions that might be expected in a bearing in run-up and run-down, the tests were conducted as continuous start-stop tests with periods of acceleration, constant rotational velocity and deceleration. A graph of the variation in the rotational velocity across one start-stop cycle within the test is presented in Fig. 2; upon finishing of one cycle, the next cycle would begin immediately. One complete test is made up of 1920 start-stop cycles.

The amount of wear was characterised by mass measurements of both the pin and the disc before and after testing, measured with a balance with 0.1 mg precision. It was recognised that the mass change of both the pin and disc would also be affected by general corrosion of

Table 1
Wear test parameters of the autoclave test.

Load	4.0 kg
Sliding wear test duration	24 h
Number of start-stop cycles	1920
Number of revolutions within a cycle	117
Sliding distance during a test	14,100 m
Maximum rotational speed	200 rpm
Acceleration and deceleration periods	10 s
Disc sample diameter	30 mm
Wear track diameter in disc sample	20 mm
Pin sample diameter	10 mm
Pin sample ground end radius	50 mm

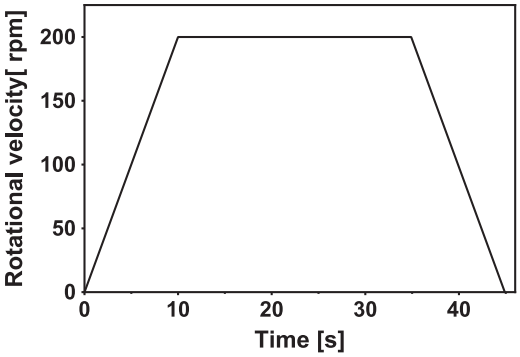

Fig. 2. Progression of the rotational velocity within one cycle in the start-stop procedure.

the surfaces which were not affected by wear (including the surfaces of the stainless steel substrates); accordingly, to assess the mass change expected to occur as a result of this general corrosion during the period of a wear test, pseudo-wear tests were conducted for 24 h at 250 °C under the same conditions as those employed in the normal wear tests, but without any mechanical contact. The mass change finally reported for the wear tests was the actual mass change during the wear tests suitably modified to remove the mass loss associated with the general corrosion of the sample surfaces not associated with wear. For tests conducted at room temperature and 80 °C, no modifications to the mass losses recorded were made; for tests conducted at 250 °C, the general corrosion mass losses recorded were 0.1 mg for the pin and 0.3 mg for the disc. Reported wear mass losses are the average of not less than two repeat tests under a given set of conditions: three, two and five tests were conducted at the temperatures of 20, 80 and 250 °C, respectively.

Wear scars on the discs were also profiled with Bruker Contour GT 3-D optical profilometer. The nature of the worn surfaces was characterised via a variety of techniques as outlined in Section 2.3.

2.3. Characterisation methods

X-ray diffraction (XRD) area measurements were conducted with Siemens D-500 using Cu-Kα radiation at 40 mA emission current and 25 kV acceleration voltage, and 0.05° step size with 2 s dwell time on each step. In seeking to understand the phase make-up in the wear track (a relatively narrow track on the disc samples), point source XRD scans were conducted with a Bruker D8-Discover using Cr-Kα radiation at 35 mA emission current and 30 kV acceleration voltage, with 0.04° step size and 4 s dwell time per step. The diameter of the nozzle used was 2 mm, which resulted in a beam maximum length of up to ~ 5 mm at the sample surface.

Porosity of polished cross-sections of the coating was measured semi-quantitatively by ImageJ [16] image analysis software in accordance with ASTM E2109-01(2007) and BS 7590:1992 standards; five fields of view were analysed. Microhardness of the polished coating cross-sections were measured with Buehler microhardness tester; an indentation load of 300 gf and a 20 s dwell time were used to make 10 indentations along the central portion of the coating section. To determine the indentation fracture toughness, indentations with a higher load of 1 kgf and a 15 s dwell time were employed to ensure that indentation cracking consistently occurred; the Evans & Wilshaw model [17] was employed:

$$K_c = 0.079\left(\frac{P}{a^{3/2}}\right)log\left(\frac{4.5a}{c}\right), \text{ for } 0.6 \leq c/a < 4.5$$

where P is the applied load, a is the indentation half diagonal and c is the indentation crack length.

Coating adhesion testing was conducted by a tensile pull-off method according to ASTM C633-13 [18], using low-carbon steel studs of 25 mm in diameter and 70 mm in length which were coated on a plane face. The coated studs were bonded to an uncoated, grit blasted stud with Araldite AV170 epoxy. Tensile loading was applied in self-aligned system so that the loading was normal to the plane of the coating. The bond strength recorded was an average of five tests.

Nanohardness measurements were conducted with a NanoTest system (Micro Materials Ltd UK) across a temperature range which fully spans that employed in the wear test programme (room temperature, 150 °C and 300 °C). All indentations were made with a maximum load of 100 mN, with indents being spaced not less than 15 μm apart.

A Nikon Eclipse LV100ND optical microscope was used for examining the wear scars in macroscale. A JEOL 6490LV scanning electron microscope (SEM) and a Philips XL30 FEG-SEM were used for observing the microstructure, and both the surfaces and the cross-sections of wear scars. An INCA energy dispersive X-ray (EDX) system was used for determining the elements present in different areas of the samples. An FEI Quanta200 3D DualBeam FIB/SEM was used for FIB milling and imaging of the milled cross-sections. Transmission electron microscopy (TEM) was conducted on a thinned FIB liftout with a JEOL JEM-2100Plus microscope with an Oxford instruments EDS system. The microscope was operated at 200 kV with a 106 μA beam current. Diffraction pattern analysis was made with CrysTBox software [19], which facilitated comparison of the measured pattern and crystallographic information files from the Crystallography Open Database [20–24].

Analysis of surfaces both outside and within the wear scar (four analyses on both areas) was conducted via X-ray photoelectron spectroscopy (XPS). Area analysis (~ 300 × 700 μm) was conducted with a Kratos AXIS ULTRA spectrometer with a monochromated Al-Kα X-ray source (1486.6 eV), operated at 120 W in electrostatic lens mode; data processing was conducted with CasaXPS software (version 2.3.19) with charge correction to the adventitious C 1s peak at 284.8 eV.

3. Results

3.1. Characterisation of the chromium oxide coating

Several methods were used to characterise the chromium oxide coating. The XRD pattern of the coating is presented in Fig. 3, and the microstructure of the cross-section in Fig. 4. The phase composition of the coating was found to be Cr_2O_3, with trace amounts of Cr_3O_4 (as identified by the minor peak at a 2θ value of 34.7° which cannot be indexed to Cr_2O_3). The porosity of the sprayed coating was determined to be 1.8 ± 0.4 vol% and its microhardness was 1220 ± 62 HV0.3. The indentation fracture toughness was 2.34 ± 0.57 MPa $m^{0.5}$ and the

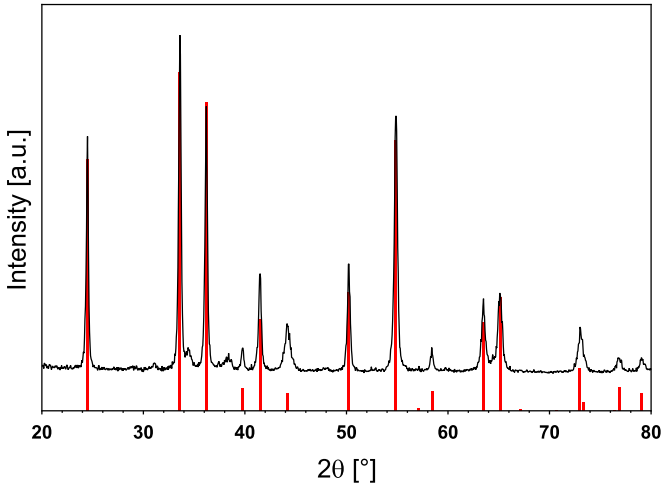

Fig. 3. XRD pattern of the chromium oxide coating in ground condition with Cr_2O_3 reference lines (Powder Diffraction File 00–038–1479 [25]).

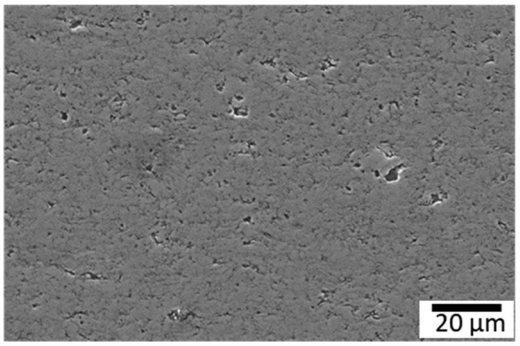

Fig. 4. Cross-section of the microstructure of the chromium oxide coating.

Table 2
Nanohardness results of chromium oxide coating obtained at room and elevated temperatures.

Temperature	Nanohardness [GPa]
Room temperature	11.8 ± 1.7
150 °C	11.9 ± 1.5
300 °C	10.8 ± 1.3

mean bond strength was 46.5 ± 3.1 MPa.

The nanohardness of the coating as a function of temperature is presented in Table 2. The nanohardness at room temperature was somewhat lower than that recorded by microhardness testing; the nanohardness did not change significantly as the temperature was raised to 150 °C, but by 300 °C, the hardness has decreased by around 10%.

3.2. Wear test results

The mass losses from both the coated pin and disc samples are presented in Fig. 5 and indicate that although wear at room temperature was very small, it increased significantly with temperature. Despite the large scatter in the results at the higher temperatures, a significant increase in wear with increasing temperature is observed.

The dependence of wear on temperature is evident also in profilometry across the wear tracks on the discs as seen in Fig. 6. At both room temperature and 80 °C, the tracks show a reduction in surface roughness compared to the material outside the track, with the wear depth at 80 °C being just slightly larger than the original surface roughness. However, following wear at 250 °C, the wear track is both much wider and deeper, commensurate with the significantly higher mass losses recorded in this case.

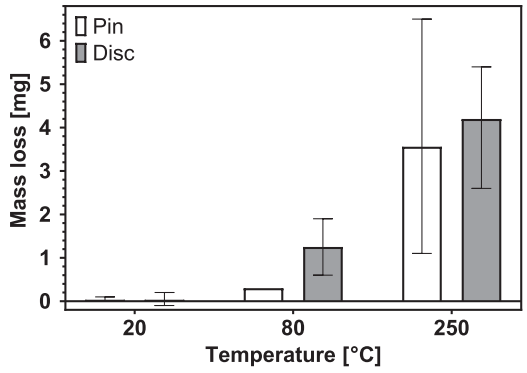

Fig. 5. Average mass loss of the samples during the tests at different temperatures with the appropriate mass change due to corrosion excluded. The error bars show minimum and maximum values at given temperature.

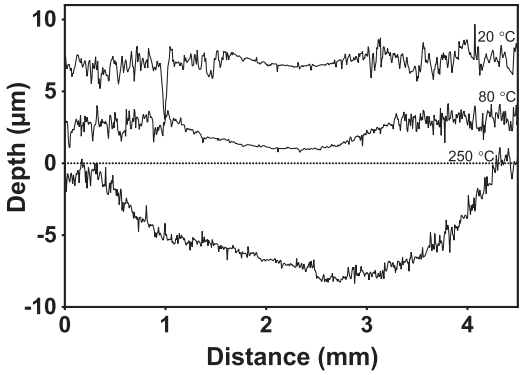

Fig. 6. Cross-section profiles of wear scars on disc samples tested at room temperature, 80 °C and 250 °C.

3.3. Wear track characterisation

Dark field optical micrographs of the wear surfaces of the pins are presented in Fig. 7. The wear scars are seen to increase in size with increasing temperature; in no cases is any coating delamination observed, but coating cracking is observed following testing at 250 °C. The wear scars were very shallow at temperatures of 80 °C and below and exhibited no cracking in either the pin or the disc samples. The most notable difference in the wear surfaces in macroscale was the presence of cracks in samples tested at 250 °C. The form of the cracks in discs was typically slightly arcing, associated with the tractional loads associated with the sliding action.

The surfaces of samples tested at the two lower temperatures (room temperature and 80 °C) were generally smooth in appearance, as indicated by the profilometry presented in Fig. 6. When observed with BSE imaging in the SEM, all wear surfaces showed the presence of a dark debris layer (the extent of which was dependent upon the test temperature), which was not present on the initial ground surface, as shown in Fig. 8; here, the wear scar with its dark debris (top of image) is contrasted with the appearance of the surface outside of the wear track (bottom of image). Higher magnification BSE images of the surfaces of the wear scars can be seen in Fig. 9 where the debris can be seen to be being retained initially in the surface roughness (grinding marks) of the original surface. The debris itself shows some signs of cracking.

In BSE imaging, the debris is clearly of lower contrast, indicating that it is a material of lower mean atomic number. EDX analysis on the surface confirms that the overall composition of the surface following wear is very similar to that before wear; spot analyses of the bright chromium oxide regions and the dark debris regions indicate a higher oxygen content in the debris (an increase of ~ 8 at%), although it is recognised that there will be significant errors associated with such analyses associated with the low atomic number of oxygen and with the interaction volume of the EDX analysis being significantly larger than the thickness of the surface debris layers being characterised. Another notable difference is that contents of up to 1 at% of some light elements were observed in the debris which were not observed in the worn chromium oxide regions. The elements identified were calcium, magnesium and aluminium, with these impurity elements originating from the coating itself, as confirmed by area analysis of cross-sections which indicates that they are present at very low levels throughout the coating.

The more surface sensitive SE-SEM images revealed that at the elevated temperatures, especially 250 °C, there appeared to be a light layer on top of the wear scar. However, this layer was not visible in BSE images, suggesting it is only very superficial, and accordingly, it was not possible to obtain compositional information of the layer via EDX analysis. It was frequently seen in the samples worn at 250 °C samples, but was also present to a smaller extent in some of the samples worn at 80 °C.

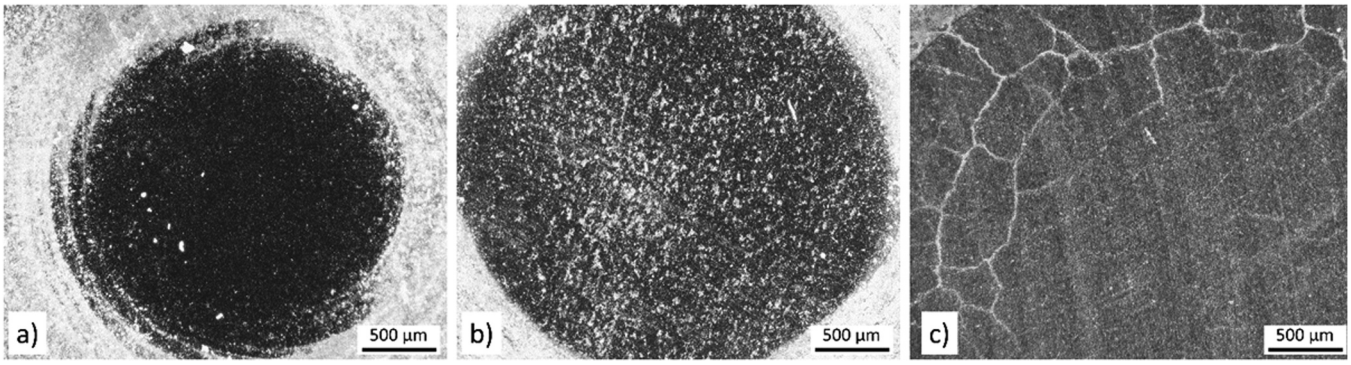

Fig. 7. Optical dark field images of pin wear surfaces tested at a) room temperature, b) 80 °C and c) 250 °C.

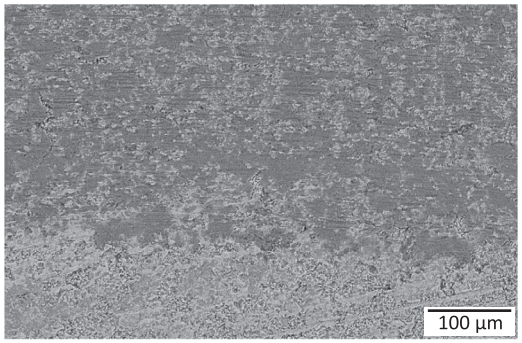

Fig. 8. Worn surface with dark debris (top of the image) and initial surface (bottom of the image) of a disc sample tested at 250 °C.

To further investigate the nature of the debris material found within the wear scars, point source XRD measurements were conducted on areas predominantly within and outside of the wear track of a disc tested at 250 °C, with the results being presented in Fig. 10. The area outside the wear track was obtained from the centre of the disc, and thus was exposed to the same corrosion conditions but was not affected by wear. It can be seen that the diffraction patterns are almost identical, indicating that the debris material is either (i) too thin to be detected by XRD; (ii) crystallographically similar to the bulk Cr_2O_3 coating; (iii) amorphous in nature.

XPS was employed in an attempt to examine if there were any chemical differences between the chromium oxide and the lower contrast debris. Again, XPS was conducted within and outside of the wear track of a disc tested at 250 °C. XPS only analyses the uppermost ~ 10 nm of the surface, and is thus dominated by the metal oxides, hydroxides and also any residual materials on the surface. Table 3 presents the data related to elements detected in this top surface for spots outside and within the wear scar; it can be seen that the overall oxygen concentration is higher within the wear scar, but also that the chromium concentration is higher, due to greater degree of surface

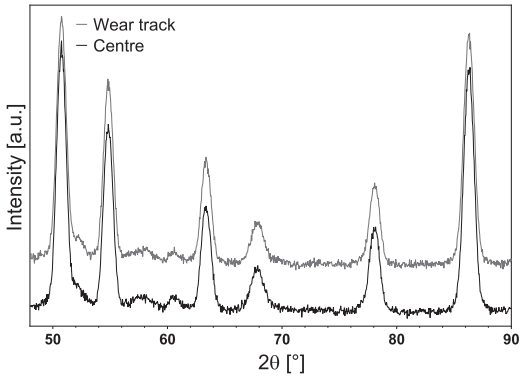

Fig. 10. XRD point source measurement with Cr-Kα radiation for areas predominantly within and outside the disc wear scar after wear testing at 250 °C.

Table 3
The average elemental composition [at%] in the top 10 nm from outside and within the wear scar (H not detectable) after wear testing at 250 °C.

Element [at%]	Outside the wear scar	Within the wear scar
O	45.3 ± 0.5	50.2 ± 0.4
C	25.9 ± 0.4	21.2 ± 0.5
N	4.0 ± 0.2	1.2 ± 0.3
Cr	23.2 ± 0.1	26.7 ± 0.4
Ca	0.6 ± 0.1	0.7 ± 0.1
Fe	0.8 ± 0.1	
Zn	0.2 ± 0.0	

contamination outside the wear scars (as indicated by the higher carbon and nitrogen levels). In the material outside the wear scar, a greater fraction of the oxygen is likely to be bonded to carbon; by use of calculations based on the work of Payne et al. [26] through deconvolution of the C 1s peak, it can be estimated that there is an increase in oxygen not associated with carbon species of approximately a fifth within the wear scar in comparison to the material outside the wear scar.

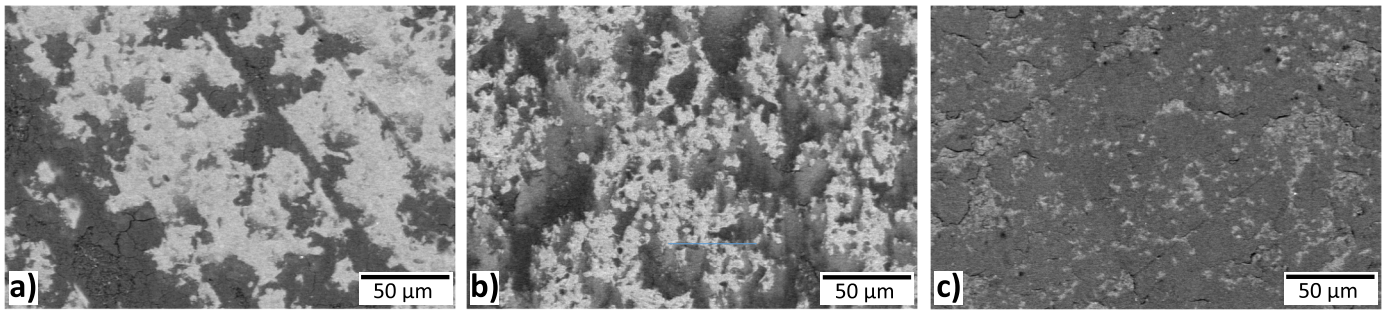

Fig. 9. Wear surfaces of disc samples tested at a) room temperature, b) 80 °C and c) 250 °C with BSE mode, showing dark debris regions in the wear track.

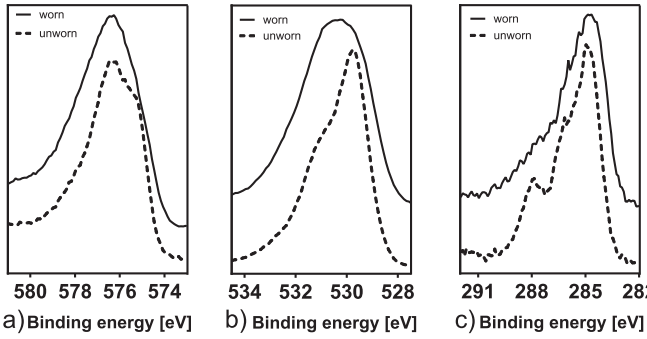

Fig. 11. Typical XPS high resolution spectra of a) chromium $2p_{3/2}$ peak, b) oxygen 1s peak and c) carbon 1s peak in worn and unworn areas after wear testing at 250 °C.

Fig. 11 presents the high resolution XPS scans of the chromium $2p_{3/2}$ peaks, oxygen 1 s peaks and carbon 1 s peaks. The chromium $2p_{3/2}$ peaks at approximately 576 eV show some shift in binding energy, which indicates the change of surface oxidation state of the chromium. The peak shapes are complex, as the Cr(III) oxidation state can have multiple splitting effects. However, simple identification suggests that the worn surface has larger hydroxide content, when deconvoluting the peaks to chromium oxide and hydroxide components; the hydroxide binding energy is higher (577.2 eV) as opposed to Cr_2O_3 binding energy (575.9–577.1 eV) [27]. It is also possible that it includes a small component of CrO_2 at lower binding energies (575.4–576.6 eV) [27], present both within and outside the wear scar. A difference can be observed in the oxygen 1 s peaks at approximately 530 eV, where a broadening and a shift to higher binding energy is seen in the wear scar when compared to the unworn region. The shift to a higher binding energy suggests a larger hydroxide content, the hydroxide binding energy being at 531.3 eV, while the chromium oxide binding energies are below 530.8 eV [27]. Fig. 11c shows the carbon 1 s peak, charge corrected to 284.8 eV. The broadening of the peak is similar in both of the scans (even though it indicates that an additional carbon species exists outside the wear scar), which indicates that the peak broadening observed in the oxygen peak is not stemming only from differences in charging of the samples.

Cross-sections through the wear scars following testing at 80 °C and 250 °C are presented in Fig. 12. In both cases, subsurface cracking can be observed, along with evidence of the debris material on the surface

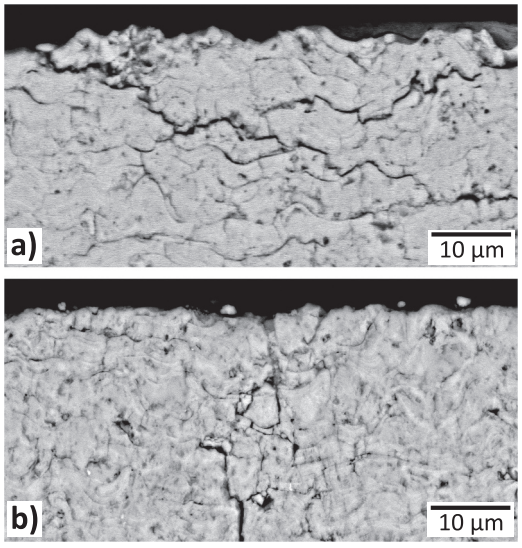

Fig. 12. Cross-sections of the disc wear scars showing a) splat boundary cracking at 80 °C, b) crack at 250 °C.

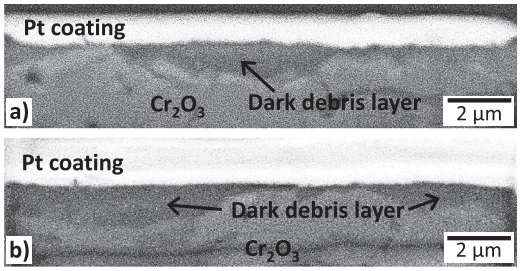

Fig. 13. FIB cross-sections of two locations in disc sample tested at 250 °C.

in Fig. 12a where it can be seen that the debris material is of the order of 1 µm in thickness. The cracking is limited to the subsurface regions of the wear scars and is therefore associated with the wear process itself (and is not just a result of thermal mismatch between the coating and the substrate).

The nature of the dark debris layers on the wear scars was investigated in more detail with focused ion beam (FIB) cross-sectioning. Two cross-sections were made of areas covered with the dark layer by first depositing a platinum strip onto the surface to protect it and then milling the side of the strip out with gallium ions, providing a view from the side when the sample was tilted. Fig. 13 shows BSE images of the two cross-sections obtained, which are both from locations within a disc wear scar tested at 250 °C. In both images, materials with three different contrast levels can be observed: the topmost, brightest area is the platinum deposited as part of the FIB process to protect the surface; directly underneath the platinum, a dark layer can be observed; the third component is the Cr_2O_3 coating, which is lighter grey. The thickness of the dark layer is not uniform, and in the locations examined, it ranges from close to zero to approximately 2–3 µm at its thickest. EDX analyses from the cross-sections resulted in similar observations to those from the EDX analyses conducted in plan view; the dark layers contained more oxygen than the light phase, and also contained small amounts of other elements (namely aluminium and calcium), which were not detectable in the lighter phase representing the Cr_2O_3 coating.

A FIB liftout of a cross-section from a wear scar area was made to examine the features present in the dark debris layer and the coating in more detail, with the FIB liftout being further thinned to allow TEM examination. Fig. 14 presents a TEM image of an area showing areas of both the dark debris layer (top of the image) and coating (bottom of the

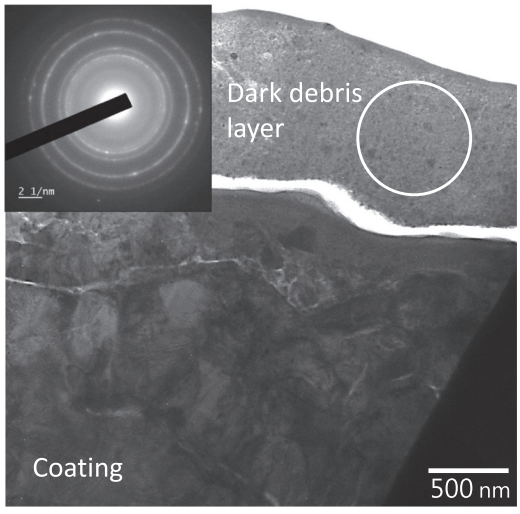

Fig. 14. TEM bright field image of a thinned FIB lift out of a cross-section through a dark debris layer following wear at 250 °C, with the dark debris layers and the bulk chromia coating clearly marked. A diffraction pattern from the marked region in the dark debris layer is presented as an inset.

image); it is noted that a crack opened during the thinning process within the debris layer itself. It can be seen that the debris layer is very fine grained in comparison to the coating, with the grain size in the debris layer being generally much less than 100 nm. The inset in Fig. 14 shows the diffraction pattern obtained from the dark debris layer; there are both clearly defined rings (indicative of a fine-grained crystalline structure) and diffuse rings close to the centre of the pattern (indicative of an amorphous structure). The ring pattern was indexed to have a good fit with Cr_2O_3 [28]. TEM-EDX verified the higher oxygen content and the higher amount of other elements like aluminium and calcium in the debris layer in comparison to the coating.

4. Discussion

The commercially-deposited chromium oxide coating examined in this work is being considered primarily in light of its combination of high corrosion resistance in autoclave conditions and its desirable mechanical properties which make it resistant to wear. As expected, the coating is made up primarily of Cr_2O_3 (Fig. 3) and exhibits the lamellar structure characteristic of thermally sprayed materials (Fig. 4). It also exhibits high hardness, although this is much less hard than many other ceramic materials employed for wear resistance alone; its indentation fracture toughness and bond strength are typical of thermally sprayed ceramic materials. Some surface cracking is observed both on the worn surface and in cross-section following wear testing (Figs. 7 and 12), but microscopy of the wear scars indicates that removal of material from the wear surfaces is attritive (Figs. 8 and 9) rather than being affected by coating delamination or cracking.

The most significant observation in this work has been the very strong dependence of the wear rate on the temperature of the lithiated water in which the test was conducted which is illustrated by both the mass loss measurements (Fig. 5) and by the profiles across the worn tracks on the disc (Fig. 6). However, the images of the wear track surfaces (Fig. 9) and cross-sections (Fig. 12) indicate that there have been no clear changes in the mechanism of material removal as would normally be expected to accompany a change in wear rate of this magnitude; the amount of dark debris on the surface, however, has increased at higher temperature. Whilst the hardness data do indicate a slight reduction in hardness (of the order of 10% - see Table 2) is to be expected as the temperature is increased from room temperature to 250 °C, such a relatively small reduction in hardness is not expected to result in the significant increase in the rate of wear observed.

It is therefore suggested that the increase in wear rate with temperature is a tribocorrosion effect, with a high degree of synergy. Corrosion of chromium containing alloys and of Cr_2O_3 itself in water at temperatures in the region 200–300 °C is known to result in the formation of a chromium oxide hydroxide, with γ-CrOOH being the preferred form at these low temperatures; γ-CrOOH is a protective (passivating) Cr(III) compound [11]. It is, therefore, suggested that γ-CrOOH forms at all the temperatures, but much more readily as the temperature is increased; moreover, it is proposed that it is readily removed by the sliding action of the pin against the disc, and thus material is removed by a continual reforming and removal of γ-CrOOH, and thus the rate of wear is governed by the rate of formation of γ-CrOOH on the surface of the Cr_2O_3.

It is clear that the dark-contrast debris formed on the surface has a higher oxygen content than the bulk of the Cr_2O_3 coating; given its thickness, the XRD evidence indicates that it is either an amorphous material or is indeed simply formed of Cr_2O_3. In addition, the TEM evidence in Fig. 14 indicates that the debris layer is made up of both an amorphous material along with crystalline Cr_2O_3, but that the grain size in the debris layer is very fine (much less than 100 nm). As such, seeking to rationalise all the evidence (both from this work and from the literature), it is suggested that the dark-contrast debris found on all of the worn tracks contains both crystalline Cr_2O_3 and amorphous γ-CrOOH which together have been retained in recesses in the surface (e.g. pre-existing grinding marks) and built up to form a debris layer. The γ-CrOOH has a lower average atomic number than the original Cr_2O_3 from which it was formed, and this explains the low contrast observed in BSE-SEM imaging. Also, it is known that γ-CrOOH is amorphous which explains why no new phases were detected by XRD when the debris-covered surface following wear at 250 °C was compared to the surface outside the wear track where there was no evidence of a debris layer (Fig. 10). Finally, the XPS data in Fig. 11 also support the proposal that the debris contains γ-CrOOH as follows; Ziemniak et al. [14] indicated that the chromium $2p_{3/2}$ peak associated with oxides of chromium are very complex to deconvolute whereas the oxygen 1s peak was different for Cr_2O_3 and CrOOH, with this difference being associated with the OH-bonded oxygen which results in a peak ~ 1.6 eV above the primary oxygen peak resulting from Cr_2O_3. The very similar behaviour observed in Fig. 11b adds weight to the evidence that the corrosion product which forms into the debris layers observed is γ-CrOOH.

The proposed mechanism of tribocorrosion is observed to result in a removal of only ~ 5–8 μm in depth from the surface of the thermally sprayed chromium oxide coating after a full test. During the test, there have been approximately 225,000 passes of the pin over the disc; it can therefore be estimated that the surface is removed at a rate of ~ 0.3 nm for every ten passes of the pin over the disc, noting that this is of the order of one atomic layer. As such, the mechanism suggested is that the surface of the Cr_2O_3 is corroded to form γ-CrOOH; this γ-CrOOH is then removed from the surface along with very fine particles of Cr_2O_3 and this mixed material is then formed into the debris layer. The kinetics of formation of γ-CrOOH are the rate determining step which explains the strong dependence of wear on temperature.

5. Conclusions

In this work, the wear behaviour of a self-mated Cr_2O_3 thermally sprayed coating pair in a water environment has been considered as a function of temperature, from room temperature to 250 °C. Under the conditions employed, the wear of this tribocouple was seen to be very small at room temperature but to increase very significantly as the temperature was increased to 250 °C. It is concluded that the increase in wear is not associated with changes in the mechanical properties of the system, but is largely a tribocorrosion effect. The Cr_2O_3 coating surfaces are damaged by both corrosion and mechanical wear, with the corrosive attack being very sensitive to temperature. At the higher temperature, a very fine-grained wear debris layer is formed which is made up of both Cr_2O_3 and γ-CrOOH. Despite the significant acceleration in the rate of wear with temperature, it is noted that under the severe test conditions employed, the depth of wear of the disc was less than 8 μm after more than 200 000 passes of the pin over the disc.

Acknowledgements

The authors gratefully acknowledge funding from Rolls-Royce plc. Mr Adam Thompson and Dr Tiziana Marrocco are acknowledged for their work in materials characterisation. This work was supported by the Engineering and Physical Sciences Research Council [grant numbers EP/K005138/1 and EP/L022494/1] United Kingdom; and the University of Nottingham. The authors thank the Nanoscale and Microscale Research Centre (nmRC) for providing access to instrumentation. Dr Emily F. Smith of the nmRC is thanked for acquiring the XPS spectra and data interpretation, Dr Christopher D. J. Parmenter for technical assistance with the FIB sample, and Dr Nigel C. Neate for the TEM imaging. Dr Nigel C. Neate and Dr Hannah Constantin are acknowledged for setting up the point source XRD measurements.

References

[1] S. Dong, B. Song, B. Hansz, H. Liao, C. Coddet, Microstructure and properties of Cr_2O_3 coating deposited by plasma spraying and dry-ice blasting, Surf. Coat. Technol. 225 (2013) 58–65, https://doi.org/10.1016/j.surfcoat.2013.03.016.

[2] V.P. Singh, A. Sil, R. Jayaganthan, Tribological behavior of plasma sprayed Cr_2O_3-3%TiO_2 coatings, Wear 272 (2011) 149–158, https://doi.org/10.1016/j.wear.2011.08.004.

[3] Y. Xie, H.M. Hawthorne, The damage mechanisms of several plasma-sprayed ceramic coatings in controlled scratching, Wear 233–235 (1999) 293–305, https://doi.org/10.1016/S0043-1648(99)00211-2.

[4] A. Cellard, V. Garnier, G. Fantozzi, G. Baret, P. Fort, Wear resistance of chromium oxide nanostructured coatings, Ceram. Int. 35 (2009) 913–916, https://doi.org/10.1016/j.ceramint.2008.02.022.

[5] G. Bolelli, V. Cannillo, L. Lusvarghi, T. Manfredini, Wear behaviour of thermally sprayed ceramic oxide coatings, Wear 261 (2006) 1298–1315, https://doi.org/10.1016/j.wear.2006.03.023.

[6] C. Monticelli, A. Balbo, F. Zucchi, Corrosion and tribocorrosion behaviour of cermet and cermet/nanoscale multilayer CrN/NbN coatings, Surf. Coat. Technol. 204 (2010) 1452–1460, https://doi.org/10.1016/j.surfcoat.2009.09.046.

[7] E. Sadri, F. Ashrafizadeh, Structural characterization and mechanical properties of plasma sprayed nanostructured Cr_2O_3-Ag composite coatings, Surf. Coat. Technol. 236 (2013) 91–101, https://doi.org/10.1016/j.surfcoat.2013.09.033.

[8] J.H. Ouyang, S. Sasaki, Effects of different additives on microstructure and high-temperature tribological properties of plasma-sprayed Cr_2O_3 ceramic coatings, Wear 249 (2001) 56–67, https://doi.org/10.1016/S0043-1648(01)00530-0.

[9] I.-W. Lyo, H.-S. Ahn, D.-S. Lim, Microstructure and tribological properties of plasma-sprayed chromium oxide–molybdenum oxide composite coatings, Surf. Coat. Technol. 163–164 (2003) 413–421, https://doi.org/10.1016/S0257-8972(02)00613-8.

[10] H.-S. Ahn, O.-K. Kwon, Tribological behaviour of plasma-sprayed chromium oxide coating, Wear 225–229 (1999) 814–824, https://doi.org/10.1016/S0043-1648(98)00390-1.

[11] P. Kritzer, N. Boukis, E. Dinjus, Factors controlling corrosion in high-temperature aqueous solutions: a contribution to the dissociation and solubility data influencing corrosion processes, J. Supercrit. Fluids 15 (1999) 205–227, https://doi.org/10.1016/S0896-8446(99)00009-1.

[12] J.E. Maslar, W.S. Hurst, W.J. Bowers, J.H. Hendricks, M.I. Aquino, I. Levin, In situ Raman spectroscopic investigation of chromium surfaces under hydrothermal conditions, Appl. Surf. Sci. 180 (2001) 102–118, https://doi.org/10.1016/S0169-4332(01)00338-5.

[13] A.N. Christensen, Hydrothermal preparation and magnetic properties of alpha-CrOOH, beta-CrOOH and gamma-CrOOH, Acta Chem. Scand. A 30 (1976) 133–136, https://doi.org/10.3891/acta.chem.scand.30a-0133.

[14] S.E. Ziemniak, M.E. Jones, K.E.S. Combs, Solubility and phase behavior of Cr (III) oxides in alkaline media at elevated temperatures, J. Solut. Chem. 27 (1998) 33–65.

[15] V. Ratia, D. Zhang, M.J. Carrington, J.L. Daure, D.G. McCartney, P.H. Shipway, D.A. Stewart, The effect of temperature on sliding wear of self-mated HIPed Stellite 6 in a simulated PWR environment, Wear (2018) In Press https://doi.org/10.1016/j.wear.2018.09.012.

[16] J. Schindelin, I. Arganda-Carreras, E. Frise, V. Kaynig, M. Longair, T. Pietzsch, S. Preibisch, C. Rueden, S. Saalfeld, B. Schmid, J.Y. Tinevez, D.J. White, V. Hartenstein, K. Eliceiri, P. Tomancak, A. Cardona, Fiji: an open-source platform for biological-image analysis, Nat. Methods 9 (2012) 676–682, https://doi.org/10.1038/nmeth.2019.

[17] A.G. Evans, T.R. Wilshaw, Quasi-static solid particle damage in brittle solids. I. Observations, analysis and implications, Acta Metall. 24 (1976) 939–957.

[18] ASTM International, ASTM C633-13 Standard Test Method for Adhesion or Cohesion Strength of Thermal Spray Coatings, (2013), pp. 1–8, https://doi.org/10.1520/C0633-13.

[19] M. Klinger, More features, more tools, more CrysTBox, J. Appl. Crystallogr. 50 (2017) 1226–1234, https://doi.org/10.1107/S1600576717006793.

[20] S. Gražulis, A. Daškevič, A. Merkys, D. Chateigner, L. Lutterotti, M. Quirós, N.R. Serebryanaya, P. Moeck, R.T. Downs, A. Le Bail, Crystallography Open Database (COD): an Open-access collection of crystal structures and platform for world-wide collaboration, Nucleic Acids Res. 40 (2012) 420–427, https://doi.org/10.1093/nar/gkr900.

[21] S. Gražulis, A. Merkys, A. Vaitkus, M. Okulič-Kazarinas, Computing stoichiometric molecular composition from crystal structures, J. Appl. Crystallogr. 48 (2015) 85–91, https://doi.org/10.1107/S1600576714025904.

[22] A. Merkys, A. Vaitkus, J. Butkus, M. Okulič-Kazarinas, V. Kairys, S. Gražulis, COD::CIF::Parser: an error-correcting CIF parser for the Perl language, J. Appl. Crystallogr. 49 (2016) 292–301, https://doi.org/10.1107/S1600576715022396.

[23] R.T. Downs, M. Hall-Wallace, The American Mineralogist crystal structure database, Am. Mineral. 88 (2003) 247–250, https://doi.org/10.1016/j.expneurol.2006.01.026.

[24] S. Graulis, D. Chateigner, R.T. Downs, A.F.T. Yokochi, M. Quirós, L. Lutterotti, E. Manakova, J. Butkus, P. Moeck, A. Le Bail, Crystallography Open Database - an open-access collection of crystal structures, J. Appl. Crystallogr. 42 (2009) 726–729, https://doi.org/10.1107/S0021889809016690.

[25] International Centre for Diffraction Data, Powder Diffraction File 00-038-1479 Cr_2O_3.

[26] B.P. Payne, M.C. Biesinger, N.S. McIntyre, X-ray photoelectron spectroscopy studies of reactions on chromium metal and chromium oxide surfaces, J. Electron Spectrosc. Relat. Phenom. 184 (2011) 29–37, https://doi.org/10.1016/j.elspec.2010.12.001.

[27] NIST X-ray Photoelectron SpectroscopyDatabase, NIST Standard ReferenceDatabase Number 20, Version 4.1, 2000. 〈http://dx.doi.org/10.18434/T4T88K〉.

[28] A. Kantor, I. Kantor, M. Merlini, K. Glazyrin, C. Prescher, M. Hanfland, L. Dubrovinsky, High-pressure structural studies of eskolaite by means of single-crystal X-ray diffraction, Am. Mineral. 97 (2012) 1764–1770, https://doi.org/10.2138/am.2012.4103.